©2025 IEEE. Personal use of this material is permitted. Permission from IEEE must be obtained for all other uses, in any current or future media, including reprinting/republishing this material for advertising or promotional purposes, creating new collective works, for resale or redistribution to servers or lists, or reuse of any copyrighted component of this work in other works.

A Triple-Phase Shift Modulation Strategy for a Dual-Active Bridge Modular Conversion System for Electrolysers

Giuseppe Bossi
Department of Electrical and Electronic Engineering
University of Cagliari
Cagliari, Italy
giuseppe.bossi@unica.it

Ariya Sangwongwanich
AAU Energy
Aalborg University
Aalborg, Denmark
ars@energy.aau.dk

Frede Blaabjerg
AAU Energy
Aalborg University
Aalborg, Denmark
fbl@energy.aau.dk

Alfonso Damiano
Department of Electrical and Electronic Engineering
University of Cagliari
Cagliari, Italy
damiano@unica.it

Abstract—**The development of green hydrogen power plants is a significant advancement in the effort to achieve net-zero carbon emissions. The employment of electrolysis systems connected to renewable energy sources via DC links plays a key role in this effort. Consequently, the implementation of novel conversion system topologies and advanced control strategies is encouraged, resulting in enhanced performance. In this contest, modular conversion systems enable system scalability and meet electrolyser's requirements concerning high current and low voltage values. In this regard, the present paper proposes a Fundamental Component Analysis-based Triple Phase Shift (FCA-TPS) modulation strategy for a Dual-Active Bridge (DAB) modular conversion system. The proposed FCA-TPS aims to suppress reverse currents on the DC link output capacitor and to mitigate harmonic content on the high frequency transformer, thus improving system efficiency. A co-simulation study and an experimental investigation on a DAB laboratory prototype validates the effectiveness of the FCA-TPS compared to SPS, achieving an efficiency value of 97.4%.**

Index Terms—**Green hydrogen, modular conversion system, dual active bridge, triple phase shift, electrolyser**

I. INTRODUCTION

Hydrogen is an essential product in several industrial sectors. The majority of hydrogen (65%) is utilised in the production of ammonia for fertilisers, with a significant proportion (25%) allocated to the synthesis of methanol for pharmaceuticals, iron production (10%) and e-mobility, energy storage and power generation (1%). The production of hydrogen typically occurs through the process of steam methane reforming (the so-called grey hydrogen) and coal gasification (black/brown hydrogen). Nonetheless, in view of the mounting worldwide emphasis on attaining net-zero carbon emissions, the generation of hydrogen through electrolysis processes utilising Renewable Energy Sources (RES) through the so-called "green hydrogen" production emerges as a promising alternative [1], [2].

The commercially available Electrolysis Systems (ELS) are characterised by low voltage and high current operating conditions. For instance, an ELS that employs the Polymer Electrolyte Membrane (PEM) stack with electrodes of $1500cm^2$ can operate up to $3kA_{DC}$ with a limited voltage range between $1.4V_{DC}$ and $2.5V_{DC}$ [2]. Consequently, the implementation of suitable power electronics to condition the power source voltage and current is imperative in order to meet the ELS requirements. Numerous interconnection schemes have been proposed in the existing literature, and the majority of commercially available ELS are grid-connected [3]. Standalone systems fed by RES are at the forefront of research activities in this field, and several advantages arise when connecting the electrolyser directly to a DC bus. For instance, the elimination of the line frequency transformer enhances overall system efficiency and facilitates greater ELS scalability and flexibility. Moreover, the interconnection to DC buses facilitates the development of enhanced converter topologies and control strategies [1], [3]. In this contest, the Dual-Active Bridge (DAB) converter represents a viable solution to efficiently interface an ELS. Indeed, the galvanic isolation provided by the high-frequency transformer (HFT) reduces noise pollution, improves electrical safety and mitigates issues related to leakage currents [2], [3]. Additionally, its features enable the development of multi-port topologies, in order to interface several energy sources independently [4].

Modular Conversion Systems (MCSs) are regarded as effective solutions for meeting the ELS requirements concerning high current and low voltage values [2]. The configuration under consideration comprises two distinct stages, as illustrated in Fig. 1. The initial stage involves the Parallel High-Voltage and Parallel Low-Voltage (PHV-PLV) connection of multiple DABs, while the second stage conditions the power towards the ELS by means of an Interleaved Buck (IB) converter. The DAB PHV-PLV stage enables the conditioning of power from an HV DC bus to a LV DC bus, thereby reducing current stress and enhancing the power rate of each DAB. Furthermore, both the HFT turn ratios and the DAB parallel connection constitute

---

This paper has been financed by the project "Ricerca di Sistema Elettrico - Accordo di Programma Ministero dell'Ambiente e della Sicurezza Energetica -ENEA Piano Triennale di Realizzazione 2022-2024, Progetto Integrato Tecnologie dell'idrogeno", CUP: I53C22003020001, and the European Union – NextGenerationEU – PROMETH2eus project-ID RSH2A_000039.

This is the accepted manuscript of the following contribution: G. Bossi, A. Sangwongwanich, F. Blaabjerg and A. Damiano, "A Triple-Phase Shift Modulation Strategy for a Dual-Active Bridge Modular Conversion System for Electrolysers," 2025 IEEE Energy Conversion Conference Congress and Exposition (ECCE), Philadelphia, PA, USA, 2025, pp. 1-8. When citing this work, please cite the original published paper: doi: 10.1109/ECCE58356.2025.11259594.

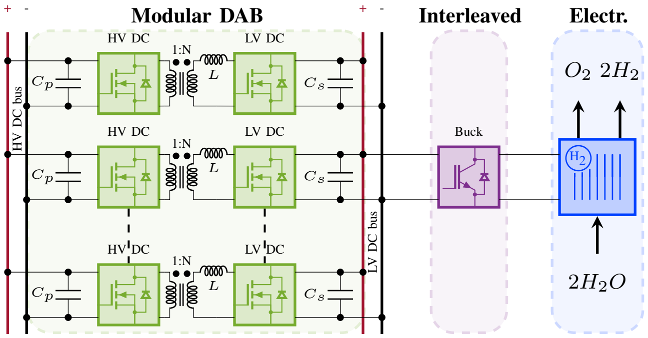

Fig. 1. The proposed parallel high voltage and parallel low voltage dual-active bridge-based modular conversion system for electrolysers.

a double degree of freedom for voltage and current scaling. Concurrently, the IB stage conditions the power from the LV DC bus to meet the ELS requirements.

The Single-Phase Shift (SPS) represents the simplest modulation strategy for DABs. The efficacy of this control strategy resides in its ability to transfer high power rates. Conversely, the non-sinusoidal current waveform exacerbates HFT core losses, while high flow-back currents in the DC-links generate a reactive power component that diminishes the converter efficiency and reduces the DC-link capacitors' lifespan. [5]–[7].

In order to overcome the aforementioned issues, Double-Phase (DPS) and Triple-Phase Shift (TPS) control strategies have been developed [5]–[8]. These approaches enable to achieve reduced current stresses on the DAB components, as well as the extension of the Zero-Voltage Switching (ZVS) operating area [9], [10].

In order to develop DPS and TPS and find the optimal control parameters, significant literature relies on a time-domain modelling approach. The utilisation of this approaches enable to model the DAB behaviour with high accuracy. Concurrently, they allow to identify the optimal working conditions for the given power requirements. On the other hand, the time-domain modelling employs complex formulations, often involving piece-wise equations, which hinders real-time working mode evaluation [11]–[13]. It is proposed that more straightforward modelling that relies on the frequency domain can be employed, which involves the Fourier expansion analysis of the converter voltage waveforms. In this regard, the Fundamental Component Analysis (FCA) represents a very simple yet accurate analysis approach [14]. In fact, the first harmonic component is responsible for almost entirely the active power content of the converter [15]–[17].

In this work, an FCA-based TPS modulation strategy (FCA-TPS) is proposed to improve the DAB conversion efficiency with a direct analytical evaluation of the optimal parameters. In particular, the FCA-TPS improves the DAB efficiency by eliminating load-side reverse currents and by reducing the harmonic content of the current in the HFT. The proposed FCA-TPS is evaluated by a co-simulation study on Matlab-Simulink and Plecs. An experimental investigation on a DAB prototype validates the co-simulation study and a comparison between the SPS and FCA-TPS efficiencies is made, thus verifying the achievement of efficiency improvement.

II. DUAL ACTIVE BRIDGE MODELLING

The DAB is a bidirectional DC-DC converter that can operate in both buck and boost modes. Its topology is shown in Fig. 2. The two full bridges interface the high-voltage (HV) and low-voltage (LV) DC buses via the DC-link capacitor banks C_p and C_s, respectively. A High-Frequency Magnetic Tank (HFMT) composed of an HFT and an external leakage inductance L_s is placed between the full bridges. Notably, L_s represents the key component for controlling the power generated in the converter.

The control strategy aims to control the flow of power from the HV DC bus to the LV DC bus. The HV DC bus fixes the voltage V_{HV} on C_p, while the control strategy establishes the LV DC voltage V_{LV} on C_s. The perturbation of V_{LV} due to the ELS power absorption produces a control response in the DAB that restores V_{LV} and meet the power requirement from the ELS. In SPS, the DAB HV and LV sides generate two two-level voltage waves v_p and v_s on the HFMT, which maximum values are equal to V_{HV} and V_{LV}, respectively. The power flow is established by imposing the unity phase shift D_0, defined as ϕ/π, between v_p and v_s. The duty cycle values of v_p and v_s, D_1 and D_2, both unified concerning the half-switching period, are fixed and set to unity. In TPS, D_1 and D_2 constitute two additional degrees of freedom that can change independently, thus enabling the control of additional aspects of the DAB. The situation depicted in Fig. 3 is established, where v_p and v_s constitute two phase-shifted three-level voltages and D_0, D_1 and D_2 can vary according to (1)

$$0 \leq D_0 \leq 0.5; \qquad 0 \leq D_1 \leq 1; \qquad 0 \leq D_2 \leq 1. \tag{1}$$

By controlling D_1 and D_2, the amplitude of v_p and v_s harmonic components is regulated, as it is shown in Fig. 3 for the fundamental component. The FCA-TPS exploits this aspect to eliminate the flow-back current on C_s and improve the harmonic content of the HFMT current. The analytical statement of the FCA-TPS is reported in the following.

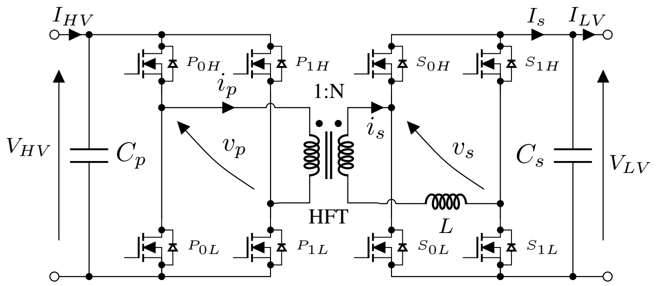

Fig. 2. Dual-active bridge topology.

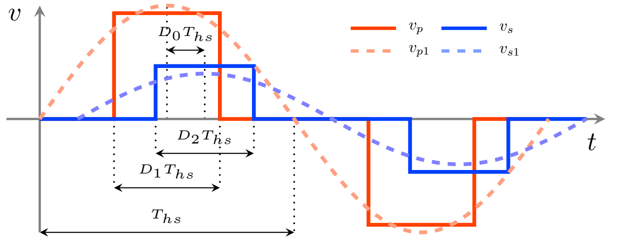

Fig. 3. High frequency magnetic tank voltages and fundamental components under triple-phase shift.

A. *Frequency-Domain Model*

The frequency-domain model relies on Fourier series expansion of v_p and v_s. Their expressions are reported in (2) and (3) reflected on the output side of the DAB HMFT

$$v_p^{''}(t) = \sum_{n=1}^{+\infty} \frac{4V_{LV}}{nM\pi} \sin(nD_1\frac{\pi}{2}) \cos(n\omega t + nD_0\pi) \tag{2}$$

$$v_s(t) = \sum_{n=1}^{+\infty} \frac{4V_{LV}}{n\pi} \sin(nD_2\frac{\pi}{2}) \cos(n\omega t) \tag{3}$$

where $n = 1, 3, 5...$ is the harmonic order, ω is the angular frequency of the voltages, t is the time and M is the DAB DC voltage gain, defined as

$$M = \frac{V_{LV}}{N\ V_{HV}}, \tag{4}$$

and N is the transformer turn ratio, defined as $v^{''}/v^{'}$. Notably, the amplitude of $v_p^{''}$ and v_s depends on the sine of D_1 and D_2, respectively. The simplified model of the DAB shown in Fig. 4 allows the statement of (5)

$$i_s(t) - i_s(0) = \frac{1}{L}\int_0^t (v_p^{''} - v_s)dt, \tag{5}$$

By replacing (2) and (3) in (5) and developing the equation, i_s is found in (6) under the hypothesis that $i_s(0) = -i_s(\pi/\omega)$

$$\begin{aligned} i_s(t) = &\sum_{n=1}^{+\infty} \frac{4V_{LV}}{n^2\pi\omega LM} \sin\left(nD_1\frac{\pi}{2}\right) \sin(n\omega t + nD_0\pi) + \\ &-\sum_{n=1}^{+\infty} \frac{4V_{LV}}{n^2\pi\omega L} \sin\left(nD_2\frac{\pi}{2}\right) \sin(n\omega t) + \\ &-\sum_{n=1}^{+\infty} \frac{4V_{LV}}{n^2\pi\omega LM} \sin\left(nD_1\frac{\pi}{2}\right) \sin(nD_0\pi) + \\ &+\frac{\pi V_{lv}}{\omega LM}D_0. \end{aligned} \tag{6}$$

The (6) can be simplified by means of the equality (7)

$$\sum_{n=1}^{+\infty} \frac{4V_{LV}}{n^2\pi\omega LM} \sin\left(nD_1\frac{\pi}{2}\right) \sin(nD_0\pi) = \frac{\pi V_{LV}}{\omega LM}D_0. \tag{7}$$

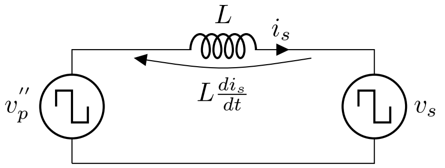

Fig. 4. Dual-active bridge simplified model concerning the fundamental voltage components.

Moreover, the algebraic sum of the sine contributions can be elaborated resorting to the symbolic representation, and the final expression of $i_s(t)$ is found in (8)

$$i_s(t) = \sum_{n=1}^{+\infty} \frac{4V_{LV}}{n^2\pi\omega LM} \sqrt{\tilde{i}_{s,A}^2 + \tilde{i}_{s,B}^2} \cos(n\omega t + \Gamma). \tag{8}$$

In (8) it is stated that i_s depends on two main factors: $\tilde{i}_{s,A}$ of (9) and $\tilde{i}_{s,B}$ of (10), that define also the phase of $i_s(t)$, Γ, as stated in (11)

$$\tilde{i}_{s,A} = \sin\left(nD_1\frac{\pi}{2}\right) \sin(nD_0\pi) \tag{9}$$

$$\tilde{i}_{s,B} = M\sin\left(nD_2\frac{\pi}{2}\right) - \sin\left(nD_1\frac{\pi}{2}\right) \cos(nD_0\pi) \tag{10}$$

$$\Gamma = \arctan\left(\frac{\tilde{i}_{s,B}}{\tilde{i}_{s,A}}\right). \tag{11}$$

Notably, the factor $\tilde{i}_{s,A}$ and $\tilde{i}_{s,B}$ depends on D_1 and D_2, which defines the amplitude of $v_p^{''}(t)$ and $v_s(t)$, respectively, and D_0. Therefore, the harmonic content of $v_p^{''}(t)$ and $v_s(t)$ characterises the harmonic content of i_s, e.g. if the amplitude of the n-th harmonic of $v_p^{''}(t)$ and $v_s(t)$ is small, the same will be also for i_s.

The HFMT active and reactive power expressions, P and Q, are stated in (12) applying the Parseval theorem:

$$P = \sum_{n=1}^{+\infty} P_n; \qquad Q = \sum_{n=1}^{+\infty} Q_n; \tag{12}$$

where P_n and Q_n are the active and reactive power contributions of each n-th harmonic component. Their expressions are evaluated by the product of (3) and (8), where n is congruent. By applying the proper mathematical simplifications and manipulations, the final expressions of P_n and Q_n are reported in (13) and (14)

$$P_n = \frac{8V_{LV}^2}{n^3\pi^2\omega LM} \sin\left(nD_2\frac{\pi}{2}\right)\ \tilde{i}_{s,A} \tag{13}$$

$$Q_n = \frac{8V_{LV}^2}{n^3\pi^2\omega LM} \sin\left(nD_2\frac{\pi}{2}\right)\ \tilde{i}_{s,B}. \tag{14}$$

Notably, P_n and Q_n depend individually by $\tilde{i}_{s,A}$ and $\tilde{i}_{s,B}$, respectively.

The Fig. 5a shows the evolution of the active power P across D_0 and the 1^{st}, 3^{rd}, 5^{th} and 7^{th} harmonic contributions, all unified over the peak value of P, $\hat{P}$. It is found that the most significant harmonic of power is the fundamental, P_1, which contributes for the 97% over P when D_0 is 0.25. In second instance, the third power component P_3 contributes for the 3.6%. Similarly, the Fig. 5b display Q and its components unified over $\hat{Q}$, founding that Q_1 contributes for the 75% and Q_3 for the 1.7% when D_0 is 0.25. Concurrently, the values Q_5 and Q_7, as well as P_5 and P_7, lie very close to 0. Therefore, it can be inferred that the fundamental component is responsible for the majority of the HFMT power and, by committing a reasonable error, the components $P_n (n > 1)$ and $Q_n (n > 1)$ are regarded as negligible.

The fundamental components of v_p'', v_s and i_s, i.e. v_{p1}'', v_{s1} and i_{s1} can be expressed in symbolic notation as reported in (15), (16) and (17)

$$\vec{v}''_{p1} = \frac{4V_{LV}}{M\pi}\sin(D_1\frac{\pi}{2})e^{jD_0\pi} \tag{15}$$

$$\vec{v}_{s1} = \frac{4V_{LV}}{\pi}\sin(D_2\frac{\pi}{2}) \tag{16}$$

$$\vec{i}_{s1} = \frac{4V_{LV}}{\pi\omega LM}\sqrt{\tilde{i}^2_{s1,A}+\tilde{i}^2_{s1,B}}\;\; e^{j\Gamma}. \tag{17}$$

The Fig. 6 shows (15), (16) and (17) when the DAB is modulated in SPS. Notably, the current factors $\tilde{i}_{s1,A}$ and $\tilde{i}_{s1,B}$ correspond to the projections of i_{s1} on the real and imaginary axis and are individually responsible for P_1 and Q_1, as stated in (13) and (14). This aspect is of particular utility in the development of the FCA-TPS modulation.

III. Fundamental Component Analysis-Based Triple Phase Shift Modulation

The objective of the FCA-TPS is the Harmonic Current Mitigation (HCM) of i_s and the Reverse Current Elimination (RCE) in C_s. The HCM can be achieved by regulating either v_p'' or v_s harmonic amplitudes, i.e. D_1 and D_2, as it is stated in (8). Concurrently, the RCE on the DC-link capacitors can be achieved by considering that the reverse currents are responsible for the reactive power in the HFMT [6]. Their quantities are affected by the modulation strategy: while in SPS the reverse currents vary concerning D_0 and cannot be managed separately, in TPS they can be regulated by the duty cycles D_1 and D_2, as it is stated in (14). Another reactive power contribution in the HFMT is represented by the magnetisation component of the transformer, that depends only on its own characteristics. However, this contribution is neglected in the DAB analytical model.

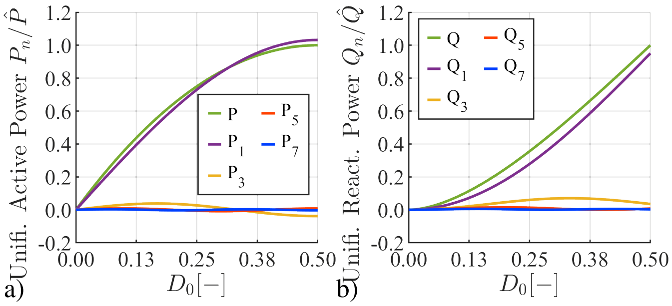

Fig. 5. Unified power and its contributions related to the 1st, 3rd, 5th and 7th harmonic components: a) active power P; b) reactive power Q.

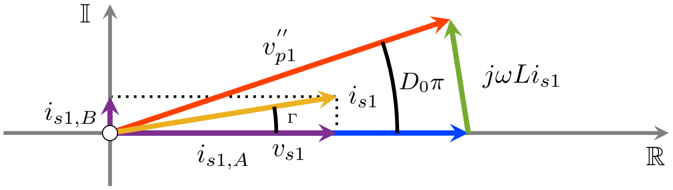

Fig. 6. Symbolic representation of v_{p1}'', v_{s1} and i_{s1} when DAB works in SPS.

Willing to make an independent action on both RCE and HCM: D_1 is dedicated to manage the RCE, while D_2 is set to achieve the HCM.

Once the FCA-TPS has been defined, the power characteristic is evaluated and the DAB control strategy is described.

A. Harmonic Current Mitigation

The cancellation of a specific v_s component of (3) allows for the mitigation of i_s harmonic spectrum and the redistribution of each n-th power contribution.

The n-th harmonic component $v_{s,n}$ is cancelled in (3) if it is applied the condition (18)

$$\sin(nD_{2_{opt,n}}\frac{\pi}{2}) = 0 \qquad \Longrightarrow \qquad D_{2_{opt,n}} = \frac{2}{n}. \tag{18}$$

By replacing (18) into (3), the THD_v is evaluated resorting to (19) as $D_{2_{opt,n}}$ varies, and the result is shown in Fig. 7.

$$THD_v = \frac{\sqrt{\sum_{n=3}^{+\infty} v_{sn}^2}}{v_{s1}}\, 100 \tag{19}$$

It is shown that the minimum THD_v is registered for $D_{2_{opt,3}}$, i.e $D_{2_{opt}} = 2/3$. Notably, the minimum THD_v is achieved by erasing the largest harmonic component after the fundamental.

B. Reverse Current Elimination

To achieve the RCE in C_s, the reactive power Q_1 must be set equal to zero. Notably, in (14) this condition is achieved if $\tilde{i}_{s1,B}$ is zero, and hence it is valid the relationship (20)

$$\tilde{i}_{s,B} = 0 \qquad \Longrightarrow \qquad \sin\left(D_1\frac{\pi}{2}\right) = \frac{\sqrt{3}M}{2\cos\left(D_0\pi\right)}, \tag{20}$$

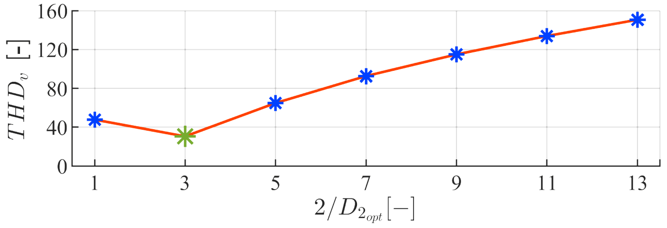

Fig. 7. Evolution of v_s's THD_v in relation to D_2.

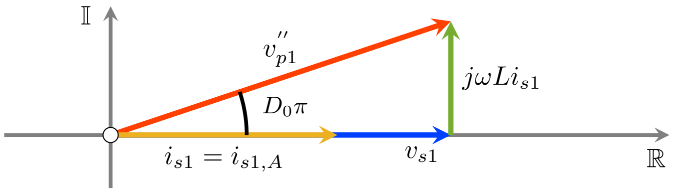

Fig. 8. Symbolic representation of v''_{p1}, v_{s1} and i_{s1} when the reverse current on the load side is eliminated employing TPS.

where $\sin\left(D_2\frac{\pi}{2}\right)$ has been evaluated concerning $D_{2_{opt}} = 2/3$. This condition is illustrated in the symbolic representation shown in Fig. 8. In particular, if $\tilde{i}_{s1,B}$ is equal to zero, then i_{s1} is equal to $i_{s1,A}$ and hence i_{s1} lies on the real axis ($\Gamma = 0$) and it has the same phase as v_{s1}. Moreover, from (20) it can be seen that at $D_0 = 0$, D_1 assumes the value of D_2 if $M = 1$, and v_{s1} corresponds to v''_{p1}. If much power is required from the DAB, the D_1 increases alongside D_0 in order to ensure that i_{s1} lies on v_{s1}. The working condition of the FCA-TPS is respected if $D_1 \leq 1$.

C. Control Strategy

The evolutions of P_1 for the FCA-TPS is found in (21) by replacing $D_{2_{opt}}$ and (20) into (13) for $n = 1$.

$$P_1 = \frac{6V_{LV}^2}{\pi^2\omega L}\tan\left(D_0\pi\right) \tag{21}$$

The maximum power $\hat{P}_1$ under FCA-TPS is achieved when D_1 reach the upper threshold of 1. In this condition, and under the hypothesis that $M = 1$, D_0 assumes the value of 1/6 concerning (20). Therefore, the constraints of the FCA-TPS shrink to (22) with respect to (1)

$$0 \leq D_0 \leq \frac{1}{6}; \qquad \frac{2}{3} \leq D_1 \leq 1; \qquad D_2 = \frac{2}{3}, \tag{22}$$

and $\hat{P}_1$ is equal to (23)

$$\hat{P}_1 = \frac{2\sqrt{3}V_{LV}^2}{\pi^2\omega L} \tag{23}$$

The DAB control strategy is based on controlling the output voltage V_{LV} on C_s. The closed-loop control scheme is reported in Fig. 9. The PI controller outcomes the D_0 phase shift by evaluating the error between the LV DC bus voltage set point $V_{LV_{set}}$ and V_{LV}. Its transfer function is reported in (24)

$$PI = k_p\frac{s + {}^{k_i}/_{k_p}}{s}. \tag{24}$$

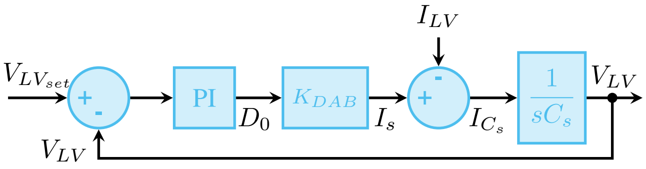

Fig. 9. Voltage control scheme for the DAB under FCA-TPS control.

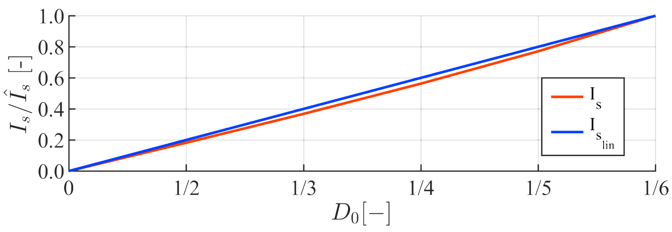

Fig. 10. DAB current model characteristic and model linearisation.

Afterwards, D_0 constitutes the input of the DAB rectified output current I_s, which constitutes the DC value of i_{s1}. The i_{s1} in the FCA-TPS is evaluated by replacing $D_{2_{opt}}$ and (20) into (17). Considering that $I_s = 2/\pi i_{s1}$, I_s is stated in (25)

$$I_s = \frac{4\sqrt{3}V_{LV}}{\pi^2\omega L}\tan\left(D_0\pi\right), \tag{25}$$

and its representation is shown in Fig. 10. In addition, the linearised characteristic of (25) is displayed in Fig. 10, which analytical expression is stated in (26)

$$I_{s_{lin}} = \frac{24V_{LV}}{\pi^2\omega L}D_0. \tag{26}$$

Both the characteristics of Fig. 10 has been unified with respect to the quantity $4V_{LV}/\pi^2\omega L$. Notably, it shows very small difference between I_s and $I_{s_{lin}}$, which makes $I_{s_{lin}}$ suitable for stability analysis and PI synthesis of the DAB controller by means of the linear theory into all the D_0 interval of existence. The I_s generated by the DAB is subtracted of the load current I_{LV} to obtain I_{C_s}, which is the current of the capacitor C_s. Lastly the output of the capacitor transfer function in Fig. 9 constitutes V_{LV} that closes the control loop.

The PI syntheses and the stability analysis is composed of two main steps: the closed-loop stability analysis and the disturbance rejection analysis. Regarding the closed-loop analysis, the open-loop and closed-loop transfer functions are evaluated in (27) and (28) considering $I_{LV} = 0$ in Fig. 9

$$G(s) = \frac{K_{DAB}k_p s + K_{DAB}k_i}{s^2 C_s} \tag{27}$$

$$W(s) = \frac{K_{DAB}k_p s + K_{DAB}k_i}{s^2 C_s + K_{DAB}k_p s + K_{DAB}k_i} \tag{28}$$

where $K_{DAB} = I_{s_{lin}}/D_0$. Concurrently, disturbance rejection analysis is performed by considering $V_{LV_{set}} = 0$, and its closed loop transfer function is reported in (29)

$$I(s) = \frac{1}{K_{DAB}k_p s + K_{DAB}k_i - C_s s^2} \tag{29}$$

Setting the DAB system parameters, the PI synthesis and the stability analysis is performed

IV. CO-IMULATION AND EXPERIMENTAL RESULTS

The co-simulation and experimental investigations were carried out based on the DAB prototype, the characteristics of which are reported in Table I. The DAB prototype is made of four half-bridge boards Imperix PEB8024 equipped with SiC MOSFETs. The boards are controlled via Imperix B-Box RCP 3.0 rapid prototyping controller that sends the PWM signals with an high-speed fibre optics system. The control algorithm is developed on Matlab/Simulink and compiled directly from the software in the controller. The HFMT comprises an HFT transformer prototype and a high-frequency inductor, both manufactured using litz wires and ferrite-based cores for high-frequency applications. The complete tests bench shown in Fig. 11. The Yokogawa DLM5058HD oscilloscope and its voltage and current probes can acquire signals at frequencies of up to 100 MHz. Meanwhile, the Yokogawa WT5000 power analyser is used to accurately measure the converter efficiency.

The DAB model has been developed using PLECS. It contemplates the actual behaviour of the SiC MOSFETs switches and the HFMT. In particular, the switches model considers the series parasitic inductance, the parallel parasitic capacitance, the drain-source on resistance and the forward voltage of the diode. Concurrently, the HFT considers both the magnetic and the electric models, while the external leakage inductance is modelled considering the series resistance of the wires. Notably, the HFT electric model, i.e. the effects of the stray capacities, represents a significant aspect, especially for high-frequency applications [18].

TABLE I
DAB Conversion System Datasheet.

DAB Main Parameters	**Values**
High Voltage Bus V_{HV}	500V
Low Voltage Bus V_{LV}	250V
HFMT Leakage Inductance L	25μH
HFMT Leakage Inductance Resistance R_L	49mΩ
Switching Frequency f_{sw}	20kHz
Dead time $t_{deadband}$	250ns
HFT Parameters	**Values**
Rated Power $\hat{P}_{HFT}$	20kW
Rated Input Voltage $\hat{V}_{DC_{HFT}}$	700V
Magnetising Inductance L_m	2mH
Input Leakage Inductance $L_{p,int}$	3.05μH
Output Leakage Inductance $L_{s,int}$	0.71μH
Turn Ration N	0.5
Input Stray Capacitance $C_{p,int}$	58pF
Inter-winding Stray Capacitance $C_{p-s,int}$	269pF
Full Bridge Imperix PEB8024 Parameters	**Values**
Rated DC-link Voltage $\hat{V}_{DC}$	800V
Rated RMS Current $\hat{I}_{AC}$ @ 20kHz, 800V	24A
Maximum Switching Frequency $\hat{f_{sw}}$ @ 800V, 12A	200kHz
DC-Link Capacitors C_p and C_s	520μF
Minimum Dead Time $\check{t}_{deadband}$	150ns
SiC Switch C2M0080120D Parameters	**Values**
Drain-Source On Resistance $R_{DS_{on}}$	88mΩ
Diode forward voltage V_f	4.1V
Series Parasitic Inductance L_{sw}	66nH
Parallel Parasitic Capacitance C_{sw}	260pF

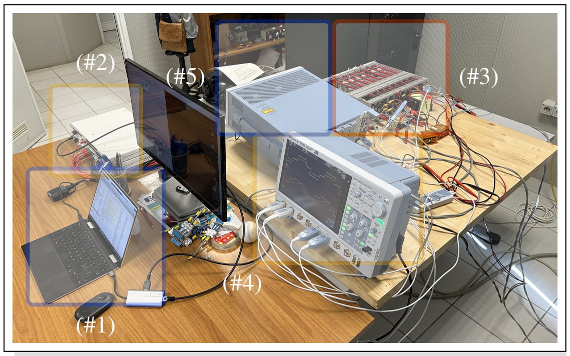

Fig. 11. Picture of the DAB prototype bench #1) PC; #2) Controller B-Box RCP 3.0; #3) DAB prototype; #4) Oscilloscope Yokogawa DLM5058HD; #5) Power analyser Yokogawa WT5000.

A. *PI Control Synthesis and Validation*

The synthesis of the PI controller for the FCA-TPS has been carried out resorting to root locus analysis. In particular, it is imposed that the poles of (28) must be real. Hence, the relationship (30) is obtained

$$k_i \leq \frac{K_{DAB} k_p^2}{4C_s}. \tag{30}$$

At the same time, the PI gains must ensure the complete disturbance rejection according to (29). By tuning $k_p = 10^{-3}$ and $k_i = 47.6\ 10^{-3}$, the constraint (30) is respected and the controller ensures system stability. The bode plots of (28) and (29) are shown in Fig. 12a and Fig. 12b, respectively. The system bandwidth is established at 70Hz and an adequate disturbance rejection is achieved.

The controller performances are evaluated in co-simulation and validated on the experimental DAB prototype. The Fig. 13 shows the evolution of the simulated and experimental waveforms of v_s and i_s after a step-load variation from 500W to 1500W (Fig. 13a) and from 2000W to 500W (Fig. 13b). Notably, it is demonstrated that the PI controller behaves as expected, with good similarity between the simulation and experimental results.

B. *Steady State Model Validation*

The Fig. 14 shows the simulated and experimental waveforms during steady-state of v_p, v_s, i_p and i_s at 500W (Fig. 14a and b) and 2000W (Fig. 14c and d). Notably, the simulation and the experimental results show good overlap, especially during the rising and falling stages. This aspects validate the proposed DAB modelling, especially concerning the effect of parasitic components in the HFT and the SiC MOSFETs.

C. *FCA-TPS Validation*

The FCA-TPS performance is validated and compared to the SPS modulation strategy. A test campaign is performed in which the power is set to 500W, 1000W, 1500W and 2000W. The v_p, v_s, i_p, i_s and the efficiency are acquired

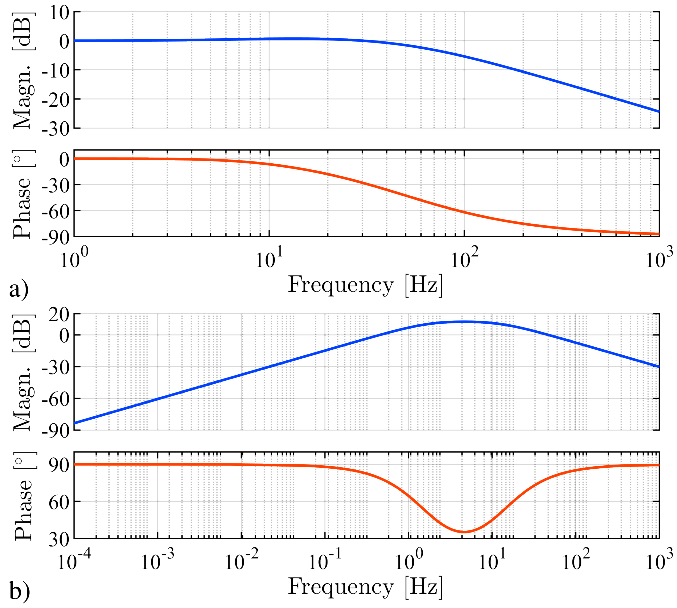

Fig. 12. Bode plots of: a) closed-loop transfer function $W(s)$; b) disturbance transfer function $I(s)$.

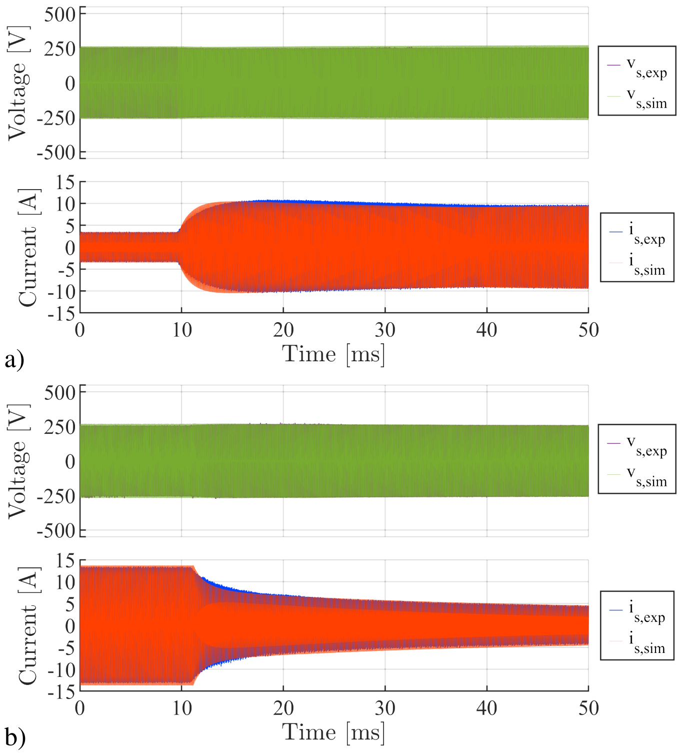

Fig. 13. Simulated and experimental signals of the HFMT output voltage and current when the load changes: a) from 500W to 1500W; b) from 2000W to 1500W.

both under FCA-TPS and SPS modulation strategies. The Fig. 15 shows the FFT harmonic spectrum of the experimental i_s. As expected, the spectra of the FCA-TPS in Fig. 15a shows enhanced harmonic content: the 3th harmonic and its multiples are cancelled, enhancing the working conditions of the HFT. The Fig. 16 shows the FFT harmonic spectrum of the HFMT output apparent power A_s. As expected, the power contribution is mostly associated to its fundamental component. Furthermore, its value is set very close to the active power contribution. This is due to the elimination of the reverse current on C_s, an effect that becomes more evident as the DAB output power increases. In fact, HFT magnetisation is more significant when DAB output power is low. Lastly, Fig. 17 shows the comparison of the efficiency characteristics of SPS and FCA-TPS, highlighting the significant improvement achieved by FCA-TPS.

V. CONCLUSION

The present paper proposes a Fundamental Component Analysis-based Triple Phase Shift (FCA-TPS) modulation strategy for a Dual-Active Bridge (DAB) modular conversion system. The proposed TPS is regarded to suppress reverse currents on the DC link output capacitor and to mitigate harmonic content on the high frequency transformer for the purpose of efficiency improvement. A co-simulation study has been conducted, and the PI controller synthesis has been performed. The experimental investigation provides the validation of the controller dynamics and the DAB modelling, with particular reference to the parasitic components of the magnetic element and the SiC MOSFETs. A comparative analysis has been conducted to assess the efficacy of the FCA-TPS in comparison to the SPS. The results indicate that the FCA-TPS exhibited enhanced efficiency, with a peak value of 97.4%.

ACKNOWLEDGMENT

This paper has been financed by the project ”Ricerca di Sistema Elettrico - Accordo di Programma Ministero dell’Ambiente e della Sicurezza Energetica -ENEA Piano Triennale di Realizzazione 2022-2024, Progetto Integrato Tecnologie dell’idrogeno”, CUP: I53C22003020001, and the European Union – NextGenerationEU – PROMETH2eus project-ID RSH2A_000039.

REFERENCES

[1] A. Hassan, O. Abdel-Rahim, M. Bajaj, and I. Zaitsev, “Power electronics for green hydrogen generation with focus on methods, topologies, and comparative analysis,” *Scientific Reports (Nature Publisher Group)*, vol. 14, no. 1, p. 24767, 2024.

[2] G. Rego, J. Rocha, J. A. Faria, J. L. Afonso, and V. Monteiro, “A Review of Hydrogen Production Methods and Power Electronics Converter Topologies for Green Hydrogen Applications,” *Energies*, vol. 17, no. 22, p. 5579, Jan. 2024.

[3] H. Renaudineau, A. M. Llor, R. Cortés D., C. A. Rojas, C. Restrepo, and S. Kouro, “Photovoltaic Green Hydrogen Challenges and Opportunities: A Power Electronics Perspective,” *IEEE Industrial Electronics Magazine*, vol. 16, no. 1, pp. 31–41, Mar. 2022.

[4] G. Bossi, M. Boi, N. Campagna, R. Miceli, and A. Damiano, “Evaluation of Triple Active Bridge for Power System of an All-Electric Aircraft.” in *2023 International Conference on Clean Electrical Power (ICCEP)*, 2023, pp. 161–166.

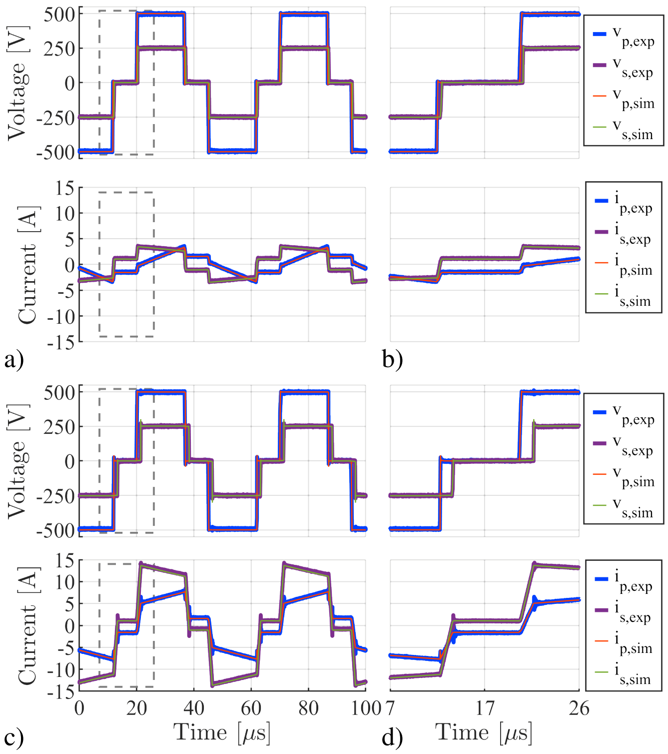

Fig. 14. FCA-TPS steady-state voltage and current waveforms inside the HFMT of the DAB: a) at 500W; b) zoom of the rising edges at 500W; a) at 2000W; b) zoom of the rising edges at 2000W;.

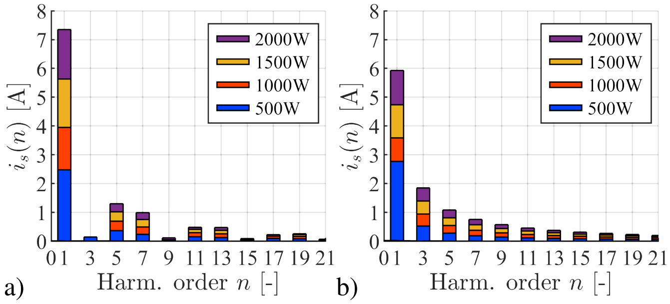

Fig. 15. FFT of the experimental HFMT output current i_s when the DAB works in: a) FCA-TPS; b) SPS.

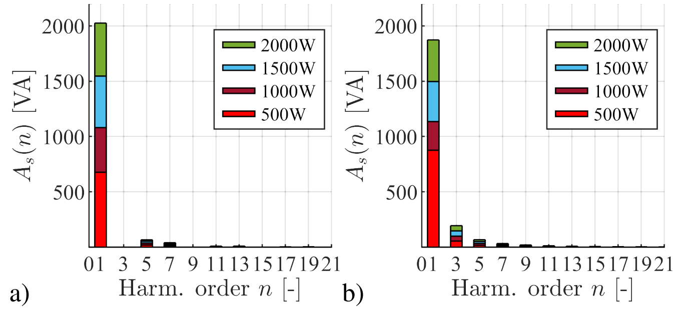

Fig. 16. HFMT output appearent power A_s evaluated from the experimental v_s and i_s signals when the DAB works in: a) FCA-TPS; b) SPS.

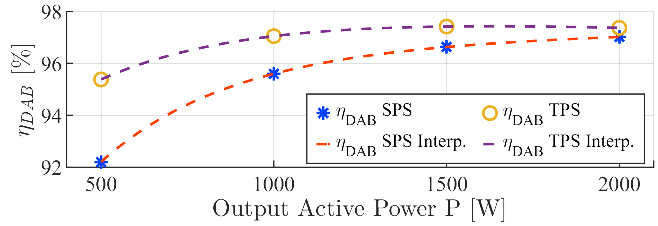

Fig. 17. Efficiency data points and their interpolations when the DAB works under SPS and FCA-TPS

[5] V. Karthikeyan, S. Rajasekar, S. Pragaspathy, and F. Blaabjerg, “Core Loss Estimation of Magnetic Links in DAB Converter Operated in High-Frequency Non-Sinusoidal Flux Waveforms,” in *2018 IEEE International Conference on Power Electronics, Drives and Energy Systems (PEDES)*, Dec. 2018, pp. 1–5.

[6] S. Shao, M. Jiang, W. Ye, Y. Li, J. Zhang, and K. Sheng, “Optimal Phase-Shift Control to Minimize Reactive Power for a Dual Active Bridge DC–DC Converter,” *IEEE Transactions on Power Electronics*, vol. 34, no. 10, pp. 10 193–10 205, Oct. 2019.

[7] S. Luo, F. Wu, and G. Wang, “Improved TPS control for DAB DC–DC converter to eliminate dual-side flow back currents,” *IET Power Electronics*, vol. 13, no. 1, pp. 32–39, 2020.

[8] G. Jean-Pierre, N. Altin, A. El Shafei, and A. Nasiri, “Efficiency Optimization of Dual Active Bridge DC– DC Converter with Triple Phase-Shift Control,” in *2020 IEEE Energy Conversion Congress and Exposition (ECCE)*, Oct. 2020, pp. 1217–1222.

[9] N. Noroozi, A. Poorfakhraei, O. Zayed, A. Elezab, N. Keshmiri, M. Narimani, and A. Emadi, “RMS Current Minimization in a SiC-Based Dual Active Bridge Converter Using Triple-Phase-Shift Modulation,” *IEEE Transactions on Industrial Electronics*, vol. 70, no. 7, pp. 7173–7182, Jul. 2023.

[10] N. Hou and Y. W. Li, “Overview and Comparison of Modulation and Control Strategies for a Nonresonant Single-Phase Dual-Active-Bridge DC–DC Converter,” *IEEE Transactions on Power Electronics*, vol. 35, no. 3, pp. 3148–3172, Mar. 2020.

[11] F. An, W. Song, K. Yang, S. Yang, and L. Ma, “A Simple Power Estimation With Triple Phase-Shift Control for the Output Parallel DAB DC–DC Converters in Power Electronic Traction Transformer for Railway Locomotive Application,” *IEEE Transactions on Transportation Electrification*, vol. 5, no. 1, pp. 299–310, Mar. 2019.

[12] D. Das and K. Basu, “Optimal Design of a Dual-Active-Bridge DC–DC Converter,” *IEEE Transactions on Industrial Electronics*, vol. 68, no. 12, pp. 12 034–12 045, Dec. 2021.

[13] G. Jean-Pierre, N. Altin, A. El Shafei, and A. Nasiri, “Overall Efficiency Improvement of a Dual Active Bridge Converter Based on Triple Phase-Shift Control,” *Energies*, vol. 15, no. 19, p. 6933, Sep. 2022.

[14] G. Bossi, C. Song, A. Sangwongwanich, F. Blaabjerg, and A. Damiano, “A Harmonic-Based Triple Phase Shift Modulation Strategy for a Dual Active Bridge Converter in an All Electric Aircraft Application,” in *2024 International Symposium on Power Electronics, Electrical Drives, Automation and Motion (SPEEDAM)*, Jun. 2024, pp. 1117–1123.

[15] B. Zhao, Q. Song, W. Liu, G. Liu, and Y. Zhao, “Universal High-Frequency-Link Characterization and Practical Fundamental-Optimal Strategy for Dual-Active-Bridge DC-DC Converter Under PWM Plus Phase-Shift Control,” *IEEE Transactions on Power Electronics*, vol. 30, no. 12, pp. 6488–6494, Dec. 2015.

[16] D. Mou, L. Yuan, Q. Luo, Y. Li, C. Liu, J. Zheng, and Z. Zhao, “Overview of Multi-Degree-of-Freedom Modulation Techniques for Dual Active Bridge Converter,” *IEEE Journal of Emerging and Selected Topics in Power Electronics*, vol. 11, no. 6, pp. 5724–5737, Dec. 2023.

[17] H. Naseem and J.-K. Seok, “Reactive Power Controller for Single Phase Dual Active Bridge DC–DC Converters,” *IEEE Access*, vol. 11, pp. 141 537–141 546, 2023.

[18] G. Bossi, A. Arshad, and A. Damiano, “Comparative Analysis of Three-Winding High-Frequency Transformer Parameter Estimation Methodologies,” in *2025 International Conference on Clean ELectrical Power (ICCEP)*, Jun. 2025.